Book Chapter

Experimental Study on the Influence of Gravitational Tilt Angle on the Spatio-Temporal Evolution of Solutocapillary Convection

Shuo Yang*, Daocheng Qin, Yupeng Zhang, Lin Xu, Yudong Fu, **Jie Cui*** and Honggang Pan

Key Laboratory of Liaoning Province for Clean Combustion Power Generation and Heating Technology, Shenyang Institute of Engineering, Shenyang 110136, China

***Corresponding Authors: Shuo Yang,** Key Laboratory of Liaoning Province for Clean Combustion Power Generation and Heating Technology, Shenyang Institute of Engineering, Shenyang 110136, China

Jie Cui, Key Laboratory of Liaoning Province for Clean Combustion Power Generation and Heating Technology, Shenyang Institute of Engineering, Shenyang 110136, China

Published **January 30, 2025**

This Book Chapter is a republication of an article published by Shuo Yang, et al. at Symmetry in November 2022. (Yang, S.; Qin, D.; Zhang, Y.; Xu, L.; Fu, Y.; Cui, J.; Pan, H. Experimental Study on the Influence of Gravitational Tilt Angle on the Spatio-Temporal Evolution of Solutocapillary Convection. Symmetry 2022, 14, 2485. https://doi.org/10.3390/sym14122485)

How to cite this book chapter: Shuo Yang, Daocheng Qin, Yupeng Zhang, Lin Xu, Yudong Fu, Jie Cui, Honggang Pan. Experimental Study on the Influence of Gravitational Tilt Angle on the Spatio-Temporal Evolution of Solutocapillary Convection. In: Top 10 Contributions in Symmetry. Hyderabad, India: Academic Reads. 2025.

Author Contributions: Project administration, S.Y.; writing—review and editing, D.Q.; investigation, Y.Z.; writing—original draft preparation, L.X.; methodology, Y.F.; investigation, J.C.; methodology, H.P. All authors have read and agreed to the published version of the manuscript.

Funding: The present work is supported financially by the National Natural Science Foundation of China under the grant of 51906163, the Science and Technology Program Foundation of Liaoning Province (2021-MS-270 and LJKZ1109), the Shenyang Science and Technology Project (No. 21-108-9-08 and No. RC210010), and the Postgraduate Education and Teaching Reform Research Project in Liaoning Province.

Conflicts of Interest: The authors declare no conflict of interest.

Abstract

This paper investigated the influence of surface internal energy instability caused by the gravitational tilt angle on solutocapillary convection. The results showed that the spatio-temporal evolution of solutocapillary convection in a non-axisymmetric liquid bridge was divided into three stages under different gravitational tilt angles, “the initiating stage near the upper corner”, “development to the intermediate height”, and “shrinking toward the bottom corner”. The non-equilibrium of the left or right interface curvature caused by internal energy instability promotes the distortion of the cell flow structure. The concentration gradient on the far-earth side increases first, due to the gravitational tilt angle. With the increasing gravitational tilt angle, the lateral extension of the cell flow is inhibited. The transverse/longitudinal velocity components are suppressed; however, the velocity gradient near the boundary is increased, and the uniformity of the velocity distribution in the center of the

liquid bridge is improved. The axial component of the Bond number decreases in a small range ($Bo' = 1 \rightarrow 0.98$) with the internal energy instability, however, which has a significant effect on surface flow. Therefore, in the initiation and development stages of solutocapillary convection, the decay rate of the Marangoni number respectively decreases and increases with the increasing Bond number. The axial component of the Bond number decreases in a small range with the internal energy instability, which has a significant effect on the solute Marangoni number (Ma_c). In the initiation stage of solutocapillary convection, the decay rate of the Ma_c decreases with the increasing Bond number. Its change law is the opposite in the development stage of solutocapillary convection.

Keywords

Gravitational Tilt Angle; Non-Axisymmetric; Solutocapillary Convection; Surface Internal Energy

1. Introduction

Solutocapillary convection is a type of Marangoni effect caused by surface tension gradients, due to an uneven concentration distribution on the interface. Therefore, the instability of the Marangoni convection caused by the temperature or concentration gradient on the free interface is the main reason for impurity segregation during crystal growth. The floating zone method is used to fabricate ultrapure semiconductor crystals. During the crystal growth, the flow and heat transfer can be simulated by a configuration called the liquid bridge, which is a mass of liquid held between two discs by surface tension. Most of the results obtained so far are about axisymmetric liquid bridges; however, this study considers the effects of non-axisymmetric perturbations on the stability. In both previous European missions (Spacelab-1 and Spacelab-Dl), an experiment on the stability of liquid bridges under mechanical perturbations was conducted. However, the experimental configuration was not exactly as expected, due to the non-concentric disk supporting the liquid bridge (Spacelab-l) [1]. This misalignment changes the stability of the non-axisymmetric liquid bridge.

Furthermore, the effect of gravitational acceleration (or gravity vibration) on the interface morphology and the stability of the Marangoni convection cannot be discarded [2]. The existing research mainly focuses on the flow transition of solutocapillary convection [3,4]. Lan et al. [5] studied the bifurcation behavior of 8 mm silicon crystal development in a single ellipsoid mirror furnace and performed three-dimensional (3D) simulations of silicon floating zone (FZ) formation. The major bifurcation was discovered to be subcritical, and the 3D mode was discovered to be the dominating flow pattern. Kawaji et al. [6] investigated the Marangoni and natural convection during the crystal growth of lysozyme and cytochrome proteins. The Marangoni convection is restrained by the aqueous protein surface. Arune et al. [7] studied the effects of the starting temperature gradient in the melt, cooling rate, and Sb composition on InSb crystal formation by the horizontal Bridgman technique. The solutocapillary convection can adjust the free surface curvature without modifying the temperature gradient or cooling rate. Yu et al. [8] used numerical simulations to investigate the impact of different solute coefficients of surface tension on the solutocapillary convection of binary mixtures in cell flow. They discovered that the influence of solute coefficients of surface tension is vital to the flow pattern generation, as well as the relationship between the wave number and fundamental oscillation frequency with the solutocapillary Reynolds number. Witkowski et al. [9] conducted a linear analysis of the stability of axisymmetric flows driven by the solute concentration gradients. They concluded that, if the surface tension gradient due to differential concentration is the only driving force, the strong concentration gradient localizes the instability within its regions but leads to instability over the whole melt on a large scale. Konstantin [10] studied the kinetics of solutocapillary convection at the interface of bubbles or droplets in heterogeneous aqueous solutions of ethanol or isopropanol. It was found that, relative to the moment when the flow flux of concentrated surfactant solutions reaches the surface, the onset of solutocapillary convection is significantly delayed. The linear stability of solutocapillary convection in small spherical shells was studied by Subramanian et al. [11]. The critical Reynolds number and degree of surface harmonics were determined by a frozen-time or quasi-steady-state linear

stability analysis, as well as the maximum growth rate of the perturbations at specified parameters. The surface roughness might be caused by the Marangoni instability. Viviani et al. [12] determined experimentally a threshold for initiating solutocapillary convection. Trofimenko et al. [13] studied the durability of solutocapillary convection caused by a localized concentration source in the presence of an insoluble surfactant adsorption layer. They discovered that the primarily axisymmetric flow is unstable in comparison to the azimuthal periodic perturbation, resulting in the appearance of surface flows with multi-vortex patterns. Mizev et al. [14] experimentally and theoretically investigated the onset and stability of buoyancy–solutocapillary convection induced by the surface-active source under an interface. The competition between buoyancy and solutocapillary convection stimulates the onset of oscillatory convection. A procedure was developed for interferometry by Zuev et al. [15], which can simultaneously visualize concentration fields and convection patterns. The self-sustained oscillatory solutocapillary convection was observed around static bubbles. Kostarev et al. [16] experimentally studied the solutocapillary convection due to a vertical surfactant concentration gradient around a gas bubble in the dual mixture of miscible fluids. Sternling and Scriven's foundational hypothesis [17] states that there are two possible modes for solutocapillary convection to take place: oscillatory and stationary [17]. Schwarzenberger et al. [18] showed that, during nonlinear development, three major building elements exist: roll cells, relaxation oscillations, and relaxation oscillation waves. In a two-phase system made of paraffin oil and water, relaxation oscillations are identified as a periodic decay and re-amplification of the interfacial convection. The existence of interfacial curvature, which imposes extra gradients of interfacial tension, aids the relaxation oscillations [19]. Wang et al. [20] investigated the mobility of two droplets in a bipolar coordinate caused by solutocapillary convection. The attraction or repulsion of droplets is determined by the droplet radius and the Marangoni number, which is an important conclusion of this work. Köllner et al. [21] investigated transient solutocapillary convection in a closed two-layer system using numerical models and additional validation experiments. During the mass transfer,

complicated convective patterns emerge, forming a cell flow structure. Savino et al. [22] used transparent organic liquids (hexamethylene and methyl alcohol) as a model system to investigate difficulties that arise during the solidification of miscible metal alloys. Professor Shevtsova's team carried out a series of numerical [23,24] and experimental [25] studies on the free-surface dynamic deformation of the liquid bridge. The occurrence of free-surface vibrations in a liquid bridge owing to oscillatory thermocapillary convection was quantitatively investigated. It was discovered that dynamic surface deformation is associated with a pressure distribution that diverges when approaching corners [23]. They estimated the necessary Reynolds numbers for the first stationary bifurcation with straight and concave interfaces and explored axisymmetric steady states in curved liquid bridges (aspect ratios > $\Gamma = 1$ and $\Gamma = 1.2$) across a wide range of contact angles [24]. In terms of experimentation, they created and constructed a new experimental approach for studying dynamical free-surface deformation. Background lighting was used to create a silhouette effect. The digital images were captured using a global thresholding approach. This approach accurately calculated the free-surface deformation in sub-micron order [25]. Shevtsova et al. [26] measured free-surface displacements owing to thermocapillary–buoyancy convection using optical imaging. They independently studied the effects of thermal expansion and surface tension fluctuation across the free surface and the fluid motion. The local mean curvature was calculated and compared to its value at equilibrium, demonstrating the importance of hydrodynamic processes. Optical imaging was used to determine the size and shape of the oscillation's amplitude and fundamental frequency [27]. Its amplitude and fundamental frequency were compared to the free-surface oscillation's corresponding values. The optical imaging indicated the same dynamics as the temperature measurements.

Compared with the axisymmetric liquid bridge, the influence of surface internal energy instability in a non-axisymmetric liquid bridge on the spatio-temporal evolution of Marangoni convection is more complicated. An experimental study was conducted on the solutocapillary convection (flow pattern,

longitudinal and transverse velocity) in an isothermal liquid bridge, under the effect of surface internal energy instability by the gravitational tilt angle in this paper. In this paper, the response law of the solute Marangoni number to the surface internal energy instability caused by the gravitational tilt angle, and the influence of surface internal energy instability on the velocity distribution in the liquid bridge, were determined. It provides a theoretical basis for the preparation of space crystal materials under extreme environments.

2. Materials

As shown in Figure 1, the experimental platform mainly includes the liquid bridge generation system, image acquisition, and analysis system. The experimental instruments include a high-speed camera (shooting rate: 5200 fps), a macro close-focus lens, Macro Probe Laowa, an adjustable laser transmitter, a moving bracket for the high-speed camera, and a liquid bridge rotating bracket. The moving bracket of the high-speed camera and liquid bridge rotating bracket can achieve synchronous rotation. In the experiment, KF96-10cSt methyl silicone oil was selected as the liquid bridge medium, and the parameters are shown in Table 1.

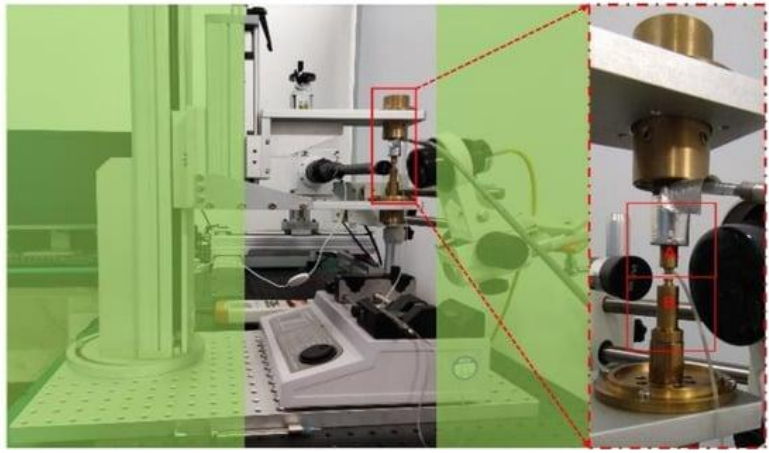

Figure 1: The experimental platform of Marangoni convection in the mesoscale liquid bridge. (A. the upper disk; B. the bottom disk.)

Table 1: Physical parameters of KF96-10cSt methyl silicone oil (T = 25 °C).

Density, ρ (kg/m^3)	**Dynamic Viscosity, μ (Pa·s)**	**Refractive Index, β (-)**	**Specific Heat, C_p (J·kg^{-1}·K^{-1})**	**Thermal Conductivity, κ (W/m·K)**	**Surface Tension, σ (mN/m)**	**Thermal Expansion Rate, γ (1/°C)**
935	9.35×10^{-3}	1.399	1672	0.14	20.1	1.06×10^{-3}

To avoid tracer particle agglomeration in the liquid bridge under the gravitational tilt angle, the dispersibility of the polyamide resin particles (the diameters of PRP1 and PRP2 are respectively d = 5 μm and d = 50 μm), fluorescent particles (PF, d = 8.5 μm), aluminum powder particles (P1, d = 10 μm) and silver-coated hollow microbeads (P2, d = 13 μm) were comprehensively investigated. The following behavior is characterized by the Stokes number (St=$\rho pD2pUl$max/18μlHSt=ρpDp2Umaxl/18μlH, where ρ_p is the particle density, g/cm^3; D_P is the particle size, and μm; UlmaxUmaxl is the maximum flow rate). This paper used the PF as the tracer particle (see Table 2 for physical parameters).

Table 2: Physical parameters of tracer particles, maximum flow rate, and St number.

Particle Type	***D*, (μm)**	**ρ, (g/cm^3)**	**β, (-)**	***Ulmax*** Umaxl**, (m/s)**	**St, (-)**
PF	8.5	3.43	2.0	1.6×10^{-3}	1.12×10^{-8}

The height of the liquid bridge is H = 2 mm; the upper and bottom disks are coaxial; and the diameter of the liquid bridge is D = 5.12 mm. The disks were designed with a 45° chamfer to prevent capillary climbing (the actual diameter of the upper and bottom disks is D = 4.88 mm). The gravitational tilt angle is φ (φ = 0°, 5°, or 10°). The left interface is the near-ground side, and the right interface is the far-ground side (see Figure 2). The experimental flow field was measured by the PIV system. The velocity field data was extracted by the open-source PIVlab.

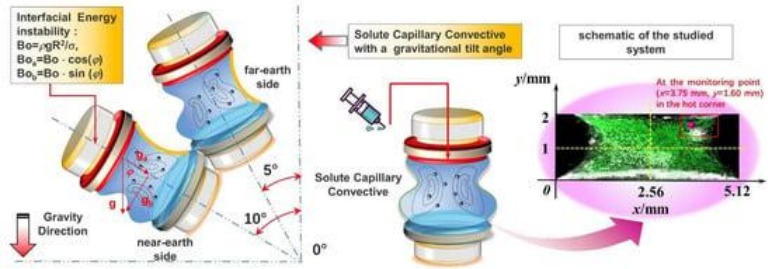

Figure 2: Solutocapillary convection of liquid bridge with the gravitational tilt angle.

3. Methods

The results of the Marangoni convection experiment with the mesoscale liquid bridge are greatly influenced by the initial experimental conditions. Therefore, the five parallel experiments on thermocapillary convection were compared to verify the operation repeatability in a certain error range. At the monitoring point (x = 3.75 mm, y = 1.60 mm) in the hot corner(as shown in Figure 2), the error analysis of the temperature difference and velocity at this point was carried out. Table 3 shows that the experiment in this paper has good repeatability.

Table 3: Parallel experiments.

No.	**The Actual Volume of a Liquid Bridge, V (μL)**	**Temperature Difference, ΔT (°C)**	**Velocity in the Hot Corner, V (m/s)**
1	23	38.5	20.0×10^{-3}
2	24	39.1	15.0×10^{-3}
3	24	40.1	15.0×10^{-3}
4	23	38.4	17.5×10^{-3}
5	23	39.6	20.0×10^{-3}
Average value	23.4	39.1	17.5×10^{-3}
Standard deviation	0.24	0.6	2.2×10^{-3}

A comparison of the current results with the available experimental data (Liang et al., 2019) [28] was done under the same conditions, by prescribing a non-isothermal liquid bridge of 5cSt silicone oil with R = 3 mm, H/R = 1, and ΔT = 9.5 °C. Figure 3 shows the distribution of the transverse velocity component along the radius at the intermediate height (the velocity was extracted by the open-source PIVlab). Although there are some differences between the two results, they have the

same order of magnitude—10^{-4}~10^{-3}. In addition, the solutocapillary convection dominated by the concentration gradient is weaker than the thermocapillary convection dominated by the temperature, so the velocity magnitude drops to 10^{-5}~10^{-4} in the following discussion.

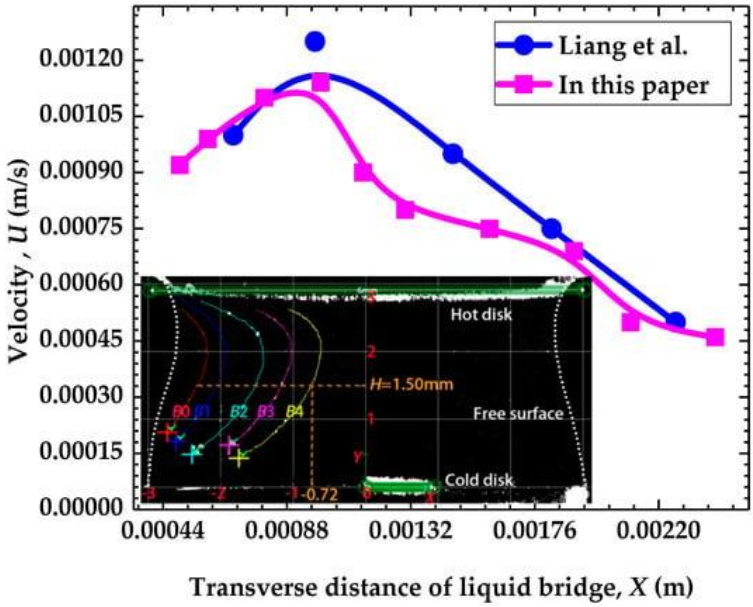

Figure 3: Transverse velocity component at the intermediate height in the left-half liquid bridge [28] (ΔT = 9.5 °C, H/R = 1, T_{amb} = 25 0 °C, D = 6 mm).

According to Ref. [29], it is vital to assess the measurement accuracy and potential mistakes in experimental dots. The maximum resolution of the high-speed camera is 1280 × 800 for the liquid bridge, with a height of 2–3 mm and diameter of D = 3~4.88 mm, which gives the accuracy of the minimum measurements' pixel pitch within 20 ± 5 μ m. In addition, the high-speed camera (Phantom VEO 410L) gives a minimum exposure of 1 ± 0.1 μs. The velocity (u) accuracy can be estimated as follows. In measuring the infinitesimal displacement and time, the relative error was assumed to be α and β, respectively. The overall error may then be calculated.

$$u = \frac{\Delta L\,(1+\alpha)}{t\,(1+\beta)} \approx \frac{\Delta L}{t} \cdot \left(1 \pm \frac{\alpha-\beta}{1+\beta}\right) \quad (1)$$

Formula (1) demonstrates that the maximum error cannot be more than $\pm(\alpha-\beta)/(1+\beta)(\alpha-\beta)/(1+\beta)$. The maximum permitted error in both infinitesimal displacement and time measurement is 13.6%.

4. Results

4.1. The Flow Characteristics of Solutocapillary Convection under the 0° Gravitational Tilt Angle

Figure 4 shows the flow pattern evolution of the solutocapillary convection under the 0° gravitational tilt angle. The area enclosed by the dotted yellow line represents the injected solute zone; the yellow arrow notes the flow direction of the cell flows; and the enclosed area with the red dotted line notes the flow structure in the annular cells. In Figure 4a,b, hexadecane was injected into the liquid bridge. Since the density of hexadecane is less than the density of 10cSt silicone oil (ρ_{sol} = 774 kg/m^3 < ρ_{10cSt} = 935 kg/m^3), the solute accumulates at the injection location (near the left of the upper disk). The solute diffuses freely along the upper disk of the liquid bridge. At the same time, the large-scale bulk flow due to the counterclockwise moving of the solute occupies the entire liquid bridge. At the time of t_2 = 36 s, the solute diffuses to the entire upper disk (as shown in Figure 4c); the solutocapillary convection forms due to the interfacial concentration gradient; and the bulk flow on the right side is separated into a reverse cell flow. Figure 4d–f shows the development of the solutocapillary convection. At the time of t_3 = 45.2 s, the solute concentration gradient increases at the upper corner, causing an uneven surface tension gradient along the free interface, as shown in Figure 4d.

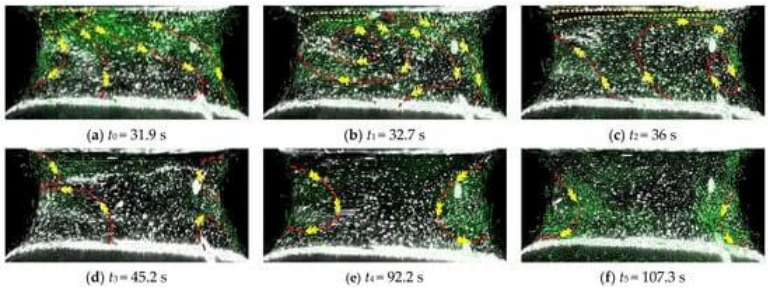

Figure 4: Spatio-temporal evolution of solutocapillary convection under the 0° gravitational tilt angle. (**a**) t_0 = 31.9 s, (**b**) t_1 = 32.7 s, (**c**) t_2 = 36 s, (**d**) t_3 = 45.2 s, (**e**) t_4 = 92.2 s, (**f**) t_5 = 107.3 s. (Vr = 0.535, Ar = 0.83, Pr = 111.667, V_{sol} = 2 μL, φ = 0°).

The surface tension of hexadecane is always greater than that of silicone oil at the same temperature (the surface tension of hexadecane and 10cSt silicone oil are, respectively, σ = 25.81 mN/m, and σ = 19.93 mN/m, at T = 25.6 °C), so the hexadecane as the solute will increase the surface tension of the local free interface. The surface tension near the upper disk is greater than that at the other positions. Therefore, the half-moon-shape cell flow ("Ↄ"-shape) is first formed near the interface at the upper corner; it is counterclockwise rotating on the left side, and it is clockwise rotating on the right side. At this time, the structure of the solutocapillary convection is small in scale, and the differentiated reverse bulk flow is below the solutocapillary convection. At the time of t_4 = 92.2 s, as the hexadecane diffuses from the upper corner to the bottom disk, the concentration gradient along the free surface gradually increases. The solutocapillary convection gradually develops and moves toward the intermediate height, as shown in Figure 4e. At the time of t_5 = 107.3 s, the solute concentration gradient gradually decreases along the liquid bridge interface. The solutocapillary convection gradually shrinks and moves to the bottom corner until it disappears (see Figure 4d). The solid lines represent the average transverse or longitudinal velocity component at the three moments (t_1' = 45.0 s, t_1'' = 45.2 s, and t_1''' = 45.4 s; t_2' = 92.0 s, t_2'' = 92.2 s, and t_2''' = 92.4 s; t_3' = 107.0 s, t_3'' = 107.3 s, and t_3''' = 107.6 s). The error band was calculated by the standard deviation between the mean and the transverse or longitudinal velocity component (t_i, t_i'', and t_i'''). In the initial stage of the

solutocapillary convection (at the time of t_3 = 45.2 s), the surface tension gradient near the upper disk is larger than that in the other positions, and it is close to the upper corner. Therefore, the average level of the transverse velocity component near the upper disk (y = 1.7 mm, y = 1.5 mm, and y = 1.2 mm) is significantly larger than that near the bottom disk (y = 0.9 mm and y = 0.6 mm). There is a set of obvious positive and negative alternating transverse velocity peaks at the height of y = 1.2 mm. As the solutocapillary convection develops, the bulk flow disappears at the time of t_4 = 92.2 s, and the solutocapillary convection moves toward the intermediate height (y = 1.2 mm), resulting in a significant variation in the transverse velocity component near the upper or bottom disk.

In Figure 5, we see that the transverse velocity decreases in the height range from y = 1.5 mm to y = 1.7 mm, and then it increases in the height range from y = 0.6 mm to y = 0.9 mm. Due to the flow pattern change to a pair of mirror-symmetric, the distribution of transverse velocity at the intermediate height approximately presents mirror symmetry, with x = 2.242 × 10^{-3} mm as the axis. At the time of t_5 = 107.3 s, as the solutocapillary convection shrinks to the bottom corner, the convection intensity weakens. The transverse velocity component is significantly attenuated (it reduces to u = 0 m/s) at the height of y = 1.5 mm~y = 1.7 mm. Because the entire cell flow is located below the intermediate height, the direction of transverse velocity is opposed to that at the time of t_3 from the height of y = 0.6 mm to y = 1.2 mm.

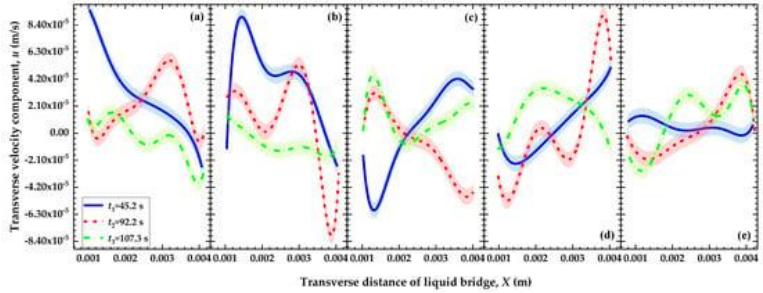

Figure 5: Distribution of transverse velocity component at the different heights under the time of t_1, t_2, and t_3. (**a**) y = 1.7 mm, (**b**) y = 1.5 mm, (**c**) y = 1.2 mm, (**d**) y = 0.9 mm, (**e**) y = 0.6 mm. (Vr = 0.535, Ar = 0.83, Pr = 111.667, V_{sol} = 2 μL).

In Figure 6, the distribution of the longitudinal velocity component at different heights is similar, and it first increases and then decays. It presents a large velocity gradient near the interface. In the initial stage (at the time of t_3 = 45.2 s), the longitudinal extension space of the solutocapillary convection is small at the upper corner. Therefore, the longitudinal velocity is close to v = 0 m/s at the heights of y = 1.5 mm~y = 1.7 mm, and its direction is negative.

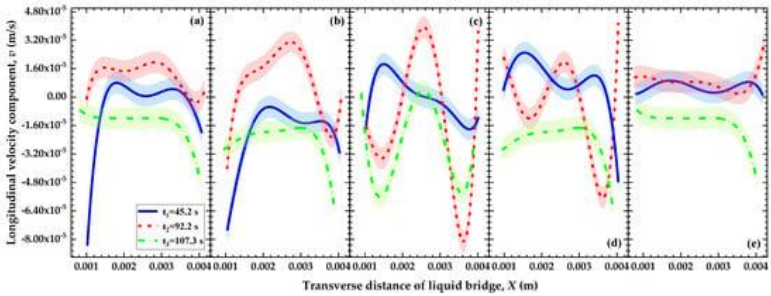

Figure 6: Distribution of longitudinal velocity component at the different heights under the time of t_1, t_2, and t_3. (**a**) y = 1.7 mm, (**b**) y = 1.5 mm, (**c**) y = 1.2 mm, (**d**) y = 0.9 mm, (**e**) y = 0.6 mm. (Vr = 0.535, Ar = 0.83, Pr = 111.667, V_{sol} = 2 μL).

At this time, the bulk flow below the solutocapillary convection occupies the most space, and the average level of the longitudinal velocity component (its direction is positive) at the height of y = 0.6 mm~y = 1.2 mm is larger than that at the height of y = 1.2 mm~y = 1.7 mm. At the time of t_4 = 92.2 s, the solutocapillary convection develops and the bulk flow disappears. The longitudinal velocity near the upper and bottom disks (y = 1.7 mm, y = 0.6 mm) is less affected by the solutocapillary convection, and it is approximately v = 0 m/s. At this time, a pair of symmetric solutocapillary convections locates in the intermedial height and occupy the entire liquid bridge. Around the intermedial height (y = 1.5 mm, y = 1.2 mm, and y = 0.9 mm), the longitudinal velocity component fluctuates wildly, and it shows a "W"-shaped distribution. The longitudinal velocity peaks at the position of x = 2.46 mm. At the time of t_5 = 107.3 s, the solutocapillary convection shrinks, and the longitudinal velocity component still maintains a large velocity gradient along the radial direction at the height of y = 1.2 mm.

4.2. The Flow Characteristics of Solutocapillary Convection under the 5° Gravitational Tilt Angle

In Figure 2, the left side of the liquid bridge is the near-earth side; the right side of the liquid bridge is the far-earth side; and the solute injection point is located at the near-earth side of the upper disk. As shown in Figure 7a,b, under the gravitational tilt angle, the solute liquid layer on the right side of the upper disk (far-earth side) is thicker than that on the left side of the upper disk (near-earth side). At the time of t_2 = 32.1 s (see Figure 7c), the solutocapillary convection is first induced on the right free surface (far-earth side) in the initial stage. The center of the large-scale bulk flow is on the left side (near-earth side). At the time of t_3 = 74.6 s (see Figure 7d), there is a pair of cell flows with different sizes on the left and right sides (compared to the 0° gravitational tilt angle), and the cell flows are near the free surface at the upper corner. At the time of t_4 = 83.6 s (see Figure 7e), the solutocapillary convection develops, and the vortex centers are located at the intermediate height. At the time of t_5 = 124.6 s (see Figure 7f), the left and right cell flows gradually shrink to the bottom corners, and the vortex center of the cell flow is away from the intermediate height. Compared to the 0° gravitational tilt angle, the solutocapillary convection has an obvious distortion, and the magnitude of the left and right cell flows is not symmetric.

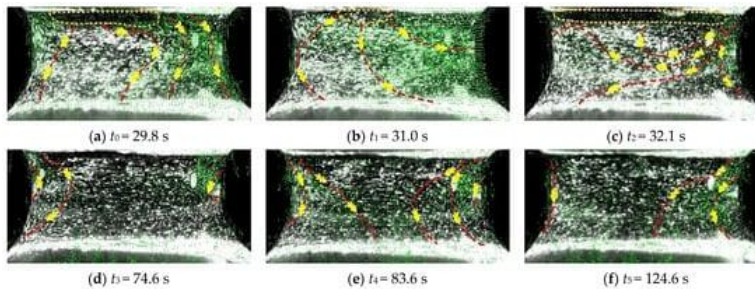

Figure 7: The spatio-temporal evolution of solutocapillary convection under the 5° gravitational tilt angle. (**a**) t_0 = 29.8 s, (**b**) t_1 = 31.0 s, (**c**) t_2 = 32.1 s, (**d**) t_3 = 74.6 s, (**e**) t_4 = 83.6 s, (**f**) t_5 = 124.6 s. (Vr = 0.535, Ar = 0.83, Pr = 111.667, V_{sol} = 2 μL, φ = 5°).

In Figure 8 and Figure 9, the solid lines represent the average transverse or longitudinal velocity component at the three moments (t_1' = 74.0 s, t_1'' = 74.6 s, and t_1''' = 75.2 s; t_2' = 83.0 s, t_2'' = 83.6 s, and t_2''' = 84.2 s; t_3' = 124.0 s, t_3'' = 124.6 s and t_3''' = 125.2 s). The error band was calculated by the standard deviation between the mean and the transverse or longitudinal velocity component (t_i, t_i'', and t_i'''). Because the surface tension gradient first increases on the right interface, the cell flow on the right free surface (far-earth side) is stronger than that on the left free surface (near-earth side). The solutocapillary convection is formed at the upper corner on the right side and the bulk flow is mainly on the left side (near-earth side). Therefore, the transverse velocity gradient on the left side (near-earth side) is smaller than that on the right side (far-earth side), as shown in Figure 8.

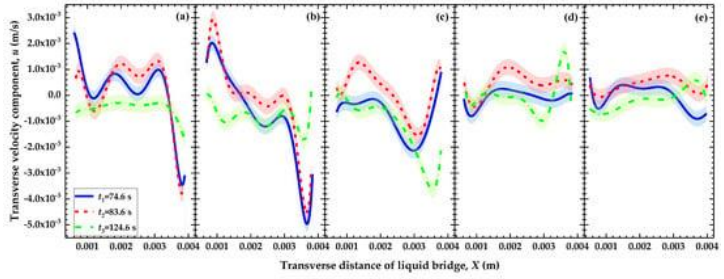

Figure 8: Distribution of transverse velocity component at the different heights under the time of t_1, t_2, and t_3. (**a**) y = 1.7 mm, (**b**) y = 1.5 mm, (**c**) y = 1.2 mm, (**d**) y = 0.9 mm, (**e**) y = 0.6 mm. (Vr = 0.535, Ar = 0.83, Pr = 111.667, D = 2.44 mm, V_{sol} = 2 μL).

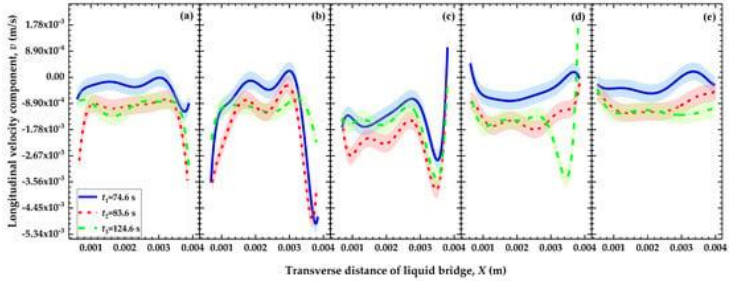

Figure 9: Distribution of longitudinal velocity component at the different heights under the time of t_1, t_2, and t_3. (**a**) y = 1.7 mm, (**b**) y = 1.5 mm, (**c**) y = 1.2 mm, (**d**) y = 0.9 mm, (**e**) y = 0.6 mm. (Vr = 0.535, Ar = 0.83, Pr = 111.667, V_{sol} = 2 μL).

The average transverse velocity component first increases and then decreases with the solutocapillary convection development, which is the same as that under the 0° gravitational tilt angle. At the initial stage (t_3 = 74.6 s), the transverse velocity component fluctuates around u = 0 m/s near the bottom disk (y = 0.6 mm~y = 0.9 mm). The peaks of transverse velocity are u_{max} = 2.47 × 10^{-3} m/s (x = 1.0 mm, y = 1.7 mm) and $|u_{max}|$ = 5.8 × 10^{-3} m/s (x = 3.5 mm, y = 1.7 mm), respectively. At the time of t_4 = 83.6 s, the average transverse velocity component increases significantly, and its direction is positive. At the height of y = 1.2 mm~y = 1.7 mm, the direction of transverse velocity shows positive and negative fluctuations. The peaks of the transverse velocity component are u_{max} = 3.7 × 10^{-3} m/s (x = 0.93 mm, y = 1.7 mm) and $|u_{max}|$ = 4.9 × 10^{-3} m/s (x = 3.6 mm, y = 1.7 mm), respectively. At the time of t_5 = 124.6 s, the cell flow on the left side (near-earth side) gradually shrinks and tends to the u = 0 m/s. The transverse velocity gradient is still larger near the right side (far-earth side). Compared with the 0° gravitational tilt angle, the right interface (far-earth side) curvature increases under the 5° gravitational tilt angle. The free surface with the large curvature inhibits the development of the cell flow on the right side, and the cell flow structure becomes flat and narrow. As a result, the longitudinal velocity gradient on the right side (far-earth side) is larger than that on the left side (near-earth side), see Figure 9. The longitudinal velocity is inhibited obviously, and its direction is negative.

4.3. The Flow Characteristics of Solutocapillary Convection under the 10° Gravitational Tilt Angle

In Figure 10a,b by further increasing the gravitational tilt angle, the solute diffusion to the upper corner on the right side (far-earth side) is intensified. The solute liquid layer on the upper disk (far-earth side) is significantly thicker than that on the left side (near-earth side). At this time (t_2 = 35.7 s), the injected solute squeezes the substrate solution (silicone oil), leading to the formation of a large-scale bulk flow (See Figure 10c). Meanwhile, the solutocapillary convection initiates from the right corner of the upper disk. Because the diffusion of the solute concentration is not uniform near the upper disk, a pair of cell

flows with different sizes is formed at the time of t_3 = 74.2 s. With the increasing right interface curvature (far-earth side), the development of the right cell flow is limited in the longitudinal direction, and it extends to the center. With the development of the solutocapillary convection (t_4 = 113.0 s), the cell flow is located at the intermediate height. The left and right cell flows are still centrally symmetric. At the time of t_5 = 137.2 s, the cell flow finally shrinks to the bottom disk, and the vortex center of the cell flow is far away from the intermediate height. Similar to the 5° gravitational tilt angles, the atrophy degree of the left and right cell flows is different due to the gravitational tilt angle.

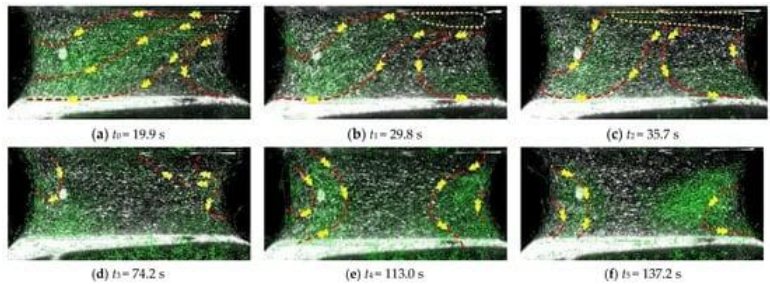

Figure 10: Spatio-temporal evolution of solutocapillary convection under the 10° gravitational tilt angle. (**a**) t_0 = 19.9 s, (**b**) t_1 = 29.8 s, (**c**) t_2 = 35.7 s, (**d**) t_3 = 74.2 s, (**e**) t_4 = 113.0 s, (**f**) t_5 = 137.2 s. (Vr = 0.535, Ar = 0.83, Pr = 111.667, V_{sol} = 2 μL, φ = 10°).

As shown in Figure 11, the transverse velocity component gradually decreases at the heights of y = 1.5 mm~y = 1.7 mm and y = 0.6 mm. With the increasing gravitational tilt angle, the transverse velocity gradient increases near the free interface at the intermediate height. The increased interface curvature causes the distribution of the transverse velocity component to shift to the left side (near-earth side). The moving of the vortex center of the cell flow influences the transverse velocity at the height of y = 0.6 mm~y = 1.2 mm, and the variation of the transverse velocity component is inhibited by the interface deformation.

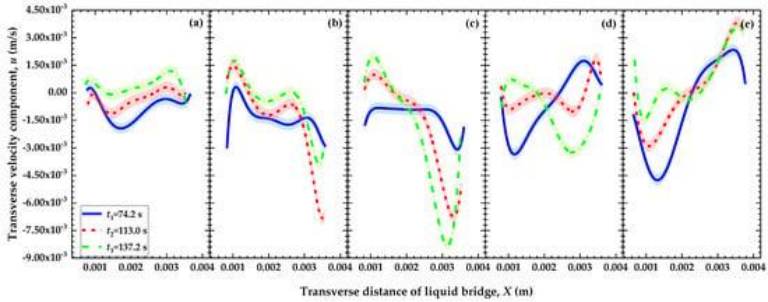

Figure 11: Distribution of transverse velocity component at the different heights under the time of t_1, t_2, and t_3. (**a**) y = 1.7 mm, (**b**) y = 1.5 mm, (**c**) y = 1.2 mm, (**d**) y = 0.9 mm, (**e**) y = 0.6 mm. (Vr = 0.535, Ar = 0.83, Pr = 111.667, D = 2.44 mm, V_{sol} = 2 μL).

As shown in Figure 12, the longitudinal velocity distribution still presents an irregular "W"-shape, and its direction is negative. The gradient of the longitudinal velocity near the free surface on the right side is larger than that on the left side, due to the increased curvature of the right interface (far-ground side). Meanwhile, the maximum longitudinal velocity occurs on the right side: $|v| = 5.7 \times 10^{-3}$ m/s (x = 3.3 mm, y = 1.2 mm, t = 113.0 s). The average longitudinal velocity first increases and then decreases with time, which is consistent with the development and shrinkage of the solutocapillary convection.

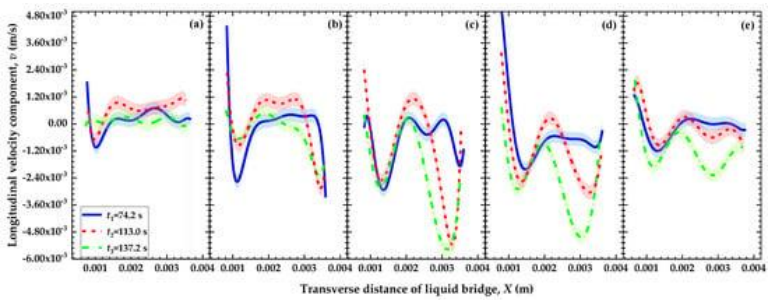

Figure 12: Distribution of longitudinal velocity component at the different heights under the time of t_1, t_2, and t_3. (**a**) y = 1.7 mm, (**b**) y = 1.5 mm, (**c**) y = 1.2 mm, (**d**) y = 0.9 mm, (**e**) y = 0.6 mm. (Vr = 0.535, Ar = 0.83, Pr = 111.667, V_{sol} = 2 μL).

Usually, surface tension is a linear function of the concentration, $\sigma_c(C) = \sigma_0(C_0) - \gamma_c(C - C_0)$, where C_0 is the solution concentration at the initial moment and $\gamma_c = (\partial\sigma_c/\partial C)|_T$, σ_0 is the surface tension at the concentration C_0 (T_0 = 25.6 °C), σ_0 = 19.93 mN/m. In this experiment, the silicone oil with 20 μL is the base solution of the liquid bridge, and the hexadecane (2 μL) is the solute. Since they don't meet the minimum solution volume of the instrument, the surface tension of the mixed solution is determined based on the similarity principle (the 3 mL hexadecane was mixed with 1 mL, 5 mL, 10 mL, and 30 mL of 10cSt silicone oil to obtain the mixed solution). As shown in Figure 13, the surface tension becomes larger with increasing concentrations, nevertheless, the variation trend of the surface tension of the liquid bridge during the solute diffusion is the opposite of the above.

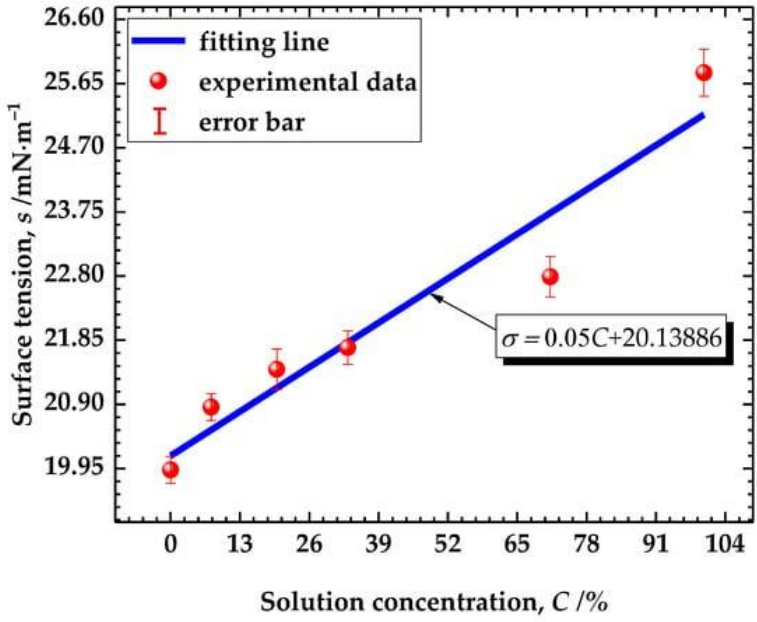

Figure 13: Variation of the surface tension with solution concentration (T_0 = 25.6 °C).

The important dimensionless parameters for the solutocapillary convection with a free surface in the present experiment are the solutal Marangoni number, as defined by $Ma_c = \gamma_c \Delta C R/\mu D_c$, where R is the characteristic length (the liquid bridge minimum radius, R = 3.6 mm), μ is the dynamic viscosity, D_c is the solute diffusivity. The dimensionless concentration is $C^* = (C - C_0)/(C_t - C_0)$. The velocity is non-dimensionalized by $\gamma_c \Delta C/\mu$. The static Bond number is $\mathbf{Bo} = \rho \mathbf{g} R^2/\sigma_0$ (the dynamic Bond number is $\mathbf{B_d} = \rho \mathbf{g} R^2/\sigma_c$), where ρ is the density difference between the liquid and the encircling medium; **g** is the gravity acceleration (a vector forming an angle (φ) with the liquid bridge's axis, see Figure 2); and σ is the surface tension. The static or dynamic Bond number has been described as a vector whose axial components match the axial components of the acceleration vector, since **g** is a vector ($Bo' = |\mathbf{Bo}|\cos\varphi = \rho g R^2 \cos\varphi/\sigma_0$ or $B_d' = |\mathbf{B_d}|\cos\varphi = \rho g R^2 \cos\varphi/\sigma_c$).

As shown in Figure 14, with the application of the gravitational tilt angle, the static Bond number gradually decreases; the buoyancy effect caused by the gravitational field weakens ($Bo' < 1$); and the interface morphology is dominated by the capillary forces. With the decay of the concentration gradient, the solute Marangoni number decreases. The axial component of the Bond number decreases in a small range by the internal energy instability, however, which has a significant effect on the Marangoni number. In the initiation stage of the solutocapillary convection, the decay rate of the Marangoni number decreases with the increasing Bond number. In the development stage of the solutocapillary convection, the decay rate of the Marangoni number increases with the increasing Bond number.

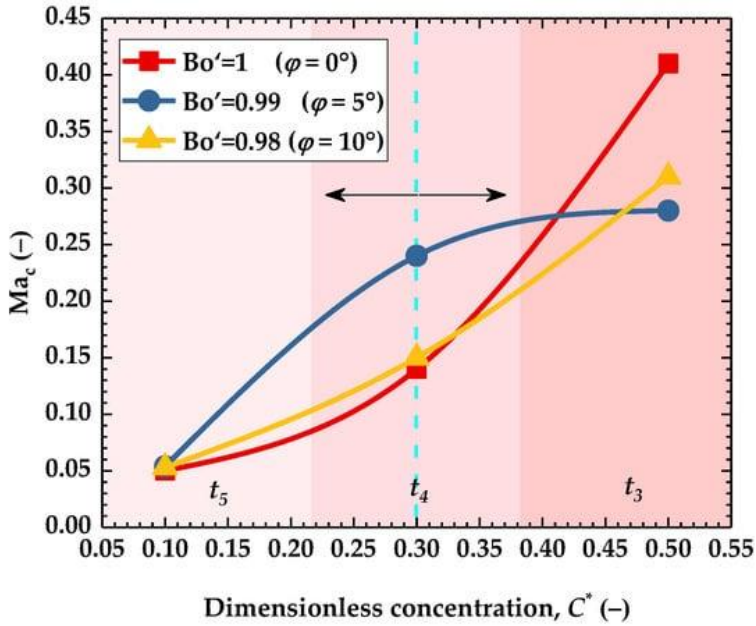

Figure 14: Variation of the solutal Marangoni number with the dimensionless concentration.

5. Conclusions

Under the influence of the solute extrusion, the bulk flow in the liquid bridge is dominant in the initial stage. With the increasing concentration gradient along the free surface height, the solutocapillary convection originates from the upper corner. The application of the gravitational tilt angle causes the initiation time lag of the solutocapillary convection. The structure of the left and right cell flows is different, and its symmetry is destroyed. Due to the increasing gravitational tilt angle (the concentration gradient first gradually increases on the right interface), the right cell flow structure is long and narrow, and the cell flow shifts to the left side. Solutocapillary convection experiences three stages: initiation, expansion, and shrinking. The increase of the interfacial curvature caused by the gravitational tilt angle is beneficial in inhibiting the development of solutocapillary convection. Meanwhile, the interface deformation restrains the lateral development of cell flow and

promotes the longitudinal flow uniformity in the central region of the liquid bridge.

With the development of solutocapillary convection, the radial distribution of transverse velocity components at different heights first increases and then decreases. The transverse velocity near the interface is smaller. Compared with the non-gravitational tilt angle, the transverse velocity has little change near the upper and bottom disks, and it is affected by the cell flow displacement at the intermediate height. With the increased right-interface curvature, the distribution of the transverse velocity shifts to the left side (near-earth side). The radial distribution of the longitudinal velocity at different heights shows an irregular "W"-shape. The longitudinal velocity decreases with the increasing gravitational tilt angle. Therefore, the surface internal energy instability caused by the gravitational tilt angle can stabilize the change of the transverse and longitudinal velocites, to a certain extent. In the initiation stage of the solutocapillary convection, the decay rate of the solute Marangoni number decreases with the surface internal energy instability. In the development of the solutocapillary convection, the decay rate of the Marangoni number increases with the surface internal energy instability.

References

1. Perales JM. Non-axisymmetric effects on long liquid bridges. Acta Astronaut. 1987; 15: 561–565.
2. Kawaji M, Liang RQ, Nasr-Esfahany M, Simic-Stefani S, Yodab S. The effect of small vibrations on Marangoni convection and the free surface of a liquid bridge. Acta Astronaut. 2006; 58: 622–632.
3. Fan JG, Liang RQ. Thermal-solutal capillary convection in binary mixture liquid bridge with various aspect ratios under microgravity. J. Cryst. Growth. 2022; 586: 126-630.
4. Benouaguef I, Musunuri N, Amah E, Blackmore D, Fischer I, et al. Solutocapillary Marangoni flow induced in a waterbody by a solute source. J. Fluid Mech. 2021; 922: A23.

5. Lan CW, Chian JH. Three-dimensional simulation of Marangoni flow and interfaces in floating-zone silicon crystal growth. J. Cryst. Growth. 2001; 230: 172–180.
6. Kawaji M, Gamache O, Hwang DH, Ichikawa N, Viola JP, et al. Investigation of Marangoni and natural convection during protein crystal growth. J. Cryst. Growth. 2003; 258: 420–430.
7. Arafune K, Kodera K, Kinoshita A, Hirata A. Control of crystal–melt interface shape during horizontal Bridgman growth of InSb crystal using solutal Marangoni convection. J. Cryst. Growth. 2003; 249: 429–436.
8. Yu JJ, Tang CY, Li YR, Tongran Q. Numerical simulation study on the pure solutocapillary flow of a binary mixture with various solutal coefficients of surface tension in an annular pool. Int. Commun. Heat Mass. 2019; 108: 104-342.
9. Witkowski LM, Walker JS. Solutocapillary instabilities in liquid bridges. Phys. Fluids. 2002; 14: 2647–2656.
10. Kostarev KG, Zuev AL, Viviani A. Experimental considerations of solutocapillary flow initiation on bubble/drop interface in the presence of a soluble surfactant. Microgravity Sci. Technol. 2009; 21: 59–65.
11. Subramanian P, Zebib A, Mcquillan B. Solutocapillary convection in spherical shells. Phys. Fluids. 2005; 17: 194–223.
12. Viviani A, Denisova M, Kostarev K, Zuev A. The threshold origin of solutocapillary Marangoni convection on a bounded free surface. Acta Astronaut. 2014; 102: 200–206.
13. Trofimenko AI, Mizev AI. Instability of solutocapillary flow in the presence of insoluble surfactant. In Proceedings of the XL International Summer School–Conference APM, St. Petersburg, Russia. 20–24 June 2012.
14. Mizev A, Birikh R. Interaction between buoyant and solutocapillary convections induced by a surface-active source placed under the free surface. Eur. Phys. J. Spec. Topics. 2011; 192: 145–153.
15. Zuev AL, Kostarev KG. Certain peculiarities of the solutocapillary convection. Physics-Uspekhi. 2008; 51: 1027–1045.

16. Kostarev K, Zuev A, Viviani A. Oscillatory Marangoni convection around the air bubble in a vertical surfactant stratification. Comptes Rendus Mec. 2004; 332: 1–7.
17. Sternling CV, Scriven LE. Interfacial turbulence: Hydrodynamic instability and the Marangoni effect. AIChE J. 1959; 5: 514–523.
18. Schwarzenberger K, Köllner T, Linde H, Boeck T, Odenbach S, et al. Pattern formation and mass transfer under stationary solutal Marangoni instability. Adv. Colloid Interface Sci. 2014; 206: 344–371.
19. Schwarzenberger K, Aland S, Domnick H, Odenbach S, Eckert K. Relaxation oscillations of solutal Marangoni convection at curved interfaces. Colloids Surf. A Physicochem. Eng. Asp. 2015; 481: 633–643.
20. Wang F, Selzer M, Nestler B. On the motion of droplets driven by solutal Marangoni convection in alloy systems with a miscibility gap. Phys. D 2015; 307: 82–96.
21. Köllner T, Schwarzenberger K, Eckert K, Boeck T. Multiscale structures in solutal Marangoni convection: Three-dimensional simulations and supporting experiments. Phys. Fluids. 2013; 25: 092-109.
22. Savino R, Piccolo C, Lappa M, Carotenuto L. Natural and Marangoni convection in partially miscible liquid systems. Acta Astronaut. 2005; 57: 89–96.
23. Shevtsova V, Ermakov MK, Ryabitskii E, Legros JC. Oscillations of a liquid bridge free surface due to the thermal convection. Acta Astronaut. 1997; 41: 471–479.
24. Shevtsova V. Thermal convection in liquid bridges with curved free surfaces: Benchmark of numerical solutions. J. Cryst. Growth. 2005; 280: 632–651.
25. Ferrera C, Mialdun A, Shevtsova V, Cabezas MG, Montanaro JM. Measurement of the dynamical free surface deformation in liquid bridges. Acta Astronaut. 2008; 62: 471–477.
26. Montanero JM, Ferrera C, Shevtsova V. Experimental study of the free surface deformation due to thermal convection in liquid bridges. Exp. Fluids. 2008; 45: 1087–1101.
27. Ferrera C, Montanero JM, Mialdun A, Shevtsova V, Cabezas MG. A new experimental technique for measuring the

dynamical free surface deformation in liquid bridges due to thermal convection. Meas. Sci. Technol. 2008; 19: 015-410.
28. Liang R, Zhou JL, Yang S, Zhang YY, Shi JH, et al. Experimental study on transition characteristics of thermo-solutocapillary convection under buoyancy. Exp. Therm. Fluid Sci. 2019; 106: 38–47.
29. Smirnov NN, Nikitin VF, Stamov LI, Tyurenkova VV, Smirnova MN. Modelling of thin wall perforation limit in debris particles impact on space structures. Acta Astronaut. 2022.